J Adv Ceram

Research Article

Reactive self-consumption strategy to suppress SiO_2 phase transition-induced cracking

Lin Chen[1], Shu-Wen Li[1], Chang-Jiu Li[1], Qiang Zhang[2], Guan-Jun Yang[1,✉]

Cite this article: Chen L, Li S, Li C, et al. *J Adv Ceram* 2025, **14**(3): 9221042. https://doi.org/10.26599/JAC.2025.9221042

ABSTRACT: The lifetime of Si bond coats in environmental barrier coatings (EBCs) is constrained by phase transition-induced cracking at the SiO_2 scale. In this study, reactive self-consumption and lattice solid solution strategies are employed to address this limitation via Si–$Yb_4Al_2O_9$ composite coatings. The formation of an $Yb_2Si_2O_7$ layer, through the consumption of the thermally grown SiO_2 scale and $Yb_4Al_2O_9$, reduces the SiO_2 thickness and significantly lowers the cracking driving force. Furthermore, the incorporation of Al into the SiO_2 lattice stabilizes high-temperature β-SiO_2, preventing phase transition-induced cracking. The proposed coating demonstrated an oxidation lifetime 20 times longer than that of pure Si at 1370 °C, highlighting its potential as an EBC bond coating.

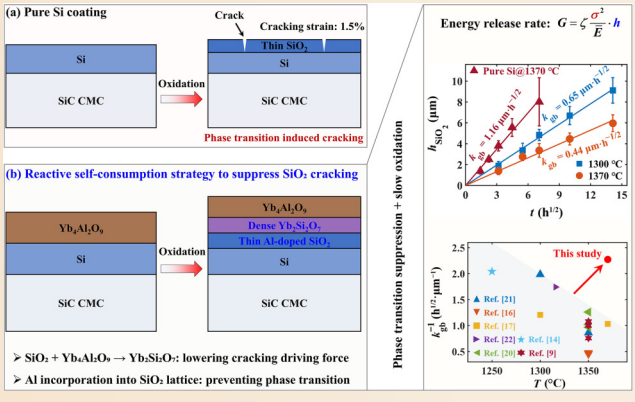

KEYWORDS: environmental barrier coatings; bond coating; oxidation; phase transition; cracking

1 Introduction

Owing to their high temperature resistance, low density, and high specific strength, ceramic matrix composites (CMCs), particularly SiC_f/SiC_m, are emerging as next-generation propulsion materials for high-pressure turbines [1–4]. SiC_f/SiC_m composites can increase engine operating temperatures by 300–500 °C and reduce engine weight by 50%–70% [5–7]. However, they are prone to rapid recession due to exposure to water vapor and oxidizers in gas turbine environments [8,9]. Environmental barrier coatings (EBCs) serve as crucial protective layers to mitigate this rapid recession [10,11]. EBCs typically comprise a Si bond coat and a rare-earth silicate ($RE_2Si_2O_7$) top coat [12]. During service at ≥ 1300 °C, a thermally grown oxide (SiO_2 TGO) forms between the Si bond coat and the top coat, which is primarily composed of β-cristobalite. However, the transition from β- to α-cristobalite occurs at approximately 220 °C, accompanied by a 4.5% volume contraction [13–15], leading to premature spalling of the EBCs. Channel cracking occurs when the thickness of SiO_2 exceeds approximately 1.5 μm [14,16], and spalling is observed along the SiO_2/Si interface when the thickness of SiO_2 reaches approximately 4 μm [14]. Therefore, suppressing the SiO_2 phase transition is crucial for ensuring the long-term operation of EBCs in turbines.

To address this phase transition issue, Si-stabilizer (such as Al_2O_3 or mullite) duplex coatings and Si–HfO_2 composite coatings have been proposed. In Si-stabilizer composite coatings [17], Al diffusion from the stabilizer to the SiO_2 scale maintains the metastability of high-temperature β-SiO_2 at room temperature, preventing phase transition-induced cracking. However, the SiO_2 growth rates in Si-stabilized composite coatings are twice as high as those in pure Si coatings at 1350 °C because of the incorporation of Al^{3+} ions into the crystalline SiO_2 lattice, which results in the formation of additional oxygen vacancies [17]. The thickness of SiO_2 TGO in Si–Al_2O_3 composite coatings reaches 23 μm after 100 h of oxidation at 1350 °C [17]. In Si–HfO_2 composite coatings [14,18–20], the suppression of phase transitions depends on the reaction between SiO_2 and HfO_2, which forms $HfSiO_4$. Nevertheless, the continuous HfO_2 phase in the composite acts as an oxygen conduit [19,21], whereas the discontinuous Si phase has a high surface area. Once Si is oxidized, the composite coating fails to provide effective protection to the SiC substrate, resulting in premature cracking along the coating/substrate interface. It has been reported that the free Si within a 50 μm thick Si–HfO_2 coating was completely oxidized within 10 h at 1371 °C [19]. Furthermore, $HfSiO_4$ has a significantly lower surface energy than the interfacial energy between $HfSiO_4$ and SiO_2, leading to phase separation between $HfSiO_4$ and SiO_2 [18]. This phase separation is detrimental to the suppression of SiO_2 cracking. These findings underscore the limitations of Si-stabilizer and Si–HfO_2 coatings in achieving long-term operation of EBCs in turbines.

[1] State Key Laboratory for Mechanical Behavior of Materials, School of Materials Science and Engineering, Xi'an Jiaotong University, Xi'an 710049, China.
[2] AECC Beijing Institute of Aeronautical Material, Beijing 100095, China.
✉ Corresponding author. E-mail: ygj@xjtu.edu.cn

Received: September 23, 2024; Revised: January 7, 2025; Accepted: February 6, 2025

Despite the rapid growth of the SiO_2 scale, Si-stabilizer duplex coatings have proven effective in suppressing the SiO_2 phase transition [22]. This study aims to inhibit both the SiO_2 phase transition and its rapid growth. To achieve this, both reactive self-consumption and lattice solid solution strategies are employed via Si–$Yb_4Al_2O_9$ composite coatings. $Yb_4Al_2O_9$ has a coefficient of thermal expansion (CTE) of 6.27×10^{-6} K^{-1} and a fracture toughness of 3.36 $MPa\cdot m^{1/2}$ [23]. Figure 1 presents a schematic illustration of the oxidation process in the Si–$Yb_4Al_2O_9$ composite coatings. Like Si-stabilizer composite coatings [10,17,24], the incorporation of Al into the SiO_2 lattice stabilizes high-temperature β-SiO_2, thereby preventing phase transition-induced cracking. Additionally, a disordered $Yb_2Si_2O_7$ layer forms through the consumption of SiO_2 and $Yb_4Al_2O_9$. $Yb_2Si_2O_7$ has an oxygen diffusion coefficient comparable to that of SiO_2 and Al_2O_3 [25], functioning as an oxygen diffusion barrier, which reduces the thickness of SiO_2 and slows its growth rate. The proposed coating exhibited an oxidation lifetime 20 times longer than that of pure Si at 1370 °C, underscoring its potential as an EBC bond coating.

2 Experimental

2.1 $Yb_4Al_2O_9$ powder preparation

The $Yb_4Al_2O_9$ powders were produced by mechanically crushing bulk $Yb_4Al_2O_9$. Initially, Yb_2O_3 and Al_2O_3 (100–200 nm, Shanghai STNANO Science & Technology Co., Ltd.) were mixed at a stoichiometric ratio of 2 : 1 via ball milling in a Si_3N_4 jar with ZrO_2 balls for 12 h at a rotation speed of 5 $r\cdot s^{-1}$. The diameter of the milling jar was 50 mm, and the ball-to-powder mass ratio was 5 : 1. Hydraulic pressing was employed to form green bodies with a diameter of 20 mm and a thickness of 3 mm, applying a pressure of 300 MPa. The dense $Yb_4Al_2O_9$ bulks were then prepared through a two-step sintering process, first at 1550 °C for 7 h, followed by 1600 °C for 8 h, with a heating and cooling rate of 5 $°C\cdot min^{-1}$. The $Yb_4Al_2O_9$ bulks were subsequently crushed in an Al_2O_3 crucible to obtain $Yb_4Al_2O_9$ powders. The particle sizes of the $Yb_4Al_2O_9$ powders ranged from 30 to 75 μm, which were achieved through mechanical screening via 200- and 400-mesh screens.

2.2 Coating preparation

In this study, pure Si, Si–$Yb_4Al_2O_9$ duplex, and Si–$Yb_4Al_2O_9$ composite coatings were prepared via a commercial atmospheric plasma spray system (APS; GP-80, Jiujiang Spraying Equipment Co., Ltd., China) equipped with a 9MBM gun (Oerlikon Metco, Switzerland) and a powder feeder (ZB80F, Hebei Zhenbang Aerospace Precision Machinery Co., Ltd., China). The APS parameters are detailed in Table 1. All the Si coatings were deposited under identical spray conditions. The particle sizes of the Si powders (Metco 4810, Oerlikon Metco, Switzerland) ranged from 30 to 75 μm. Both the Si and $Yb_4Al_2O_9$ powders exhibited irregular morphologies (Fig. 2(a)). Prior to coating deposition, the

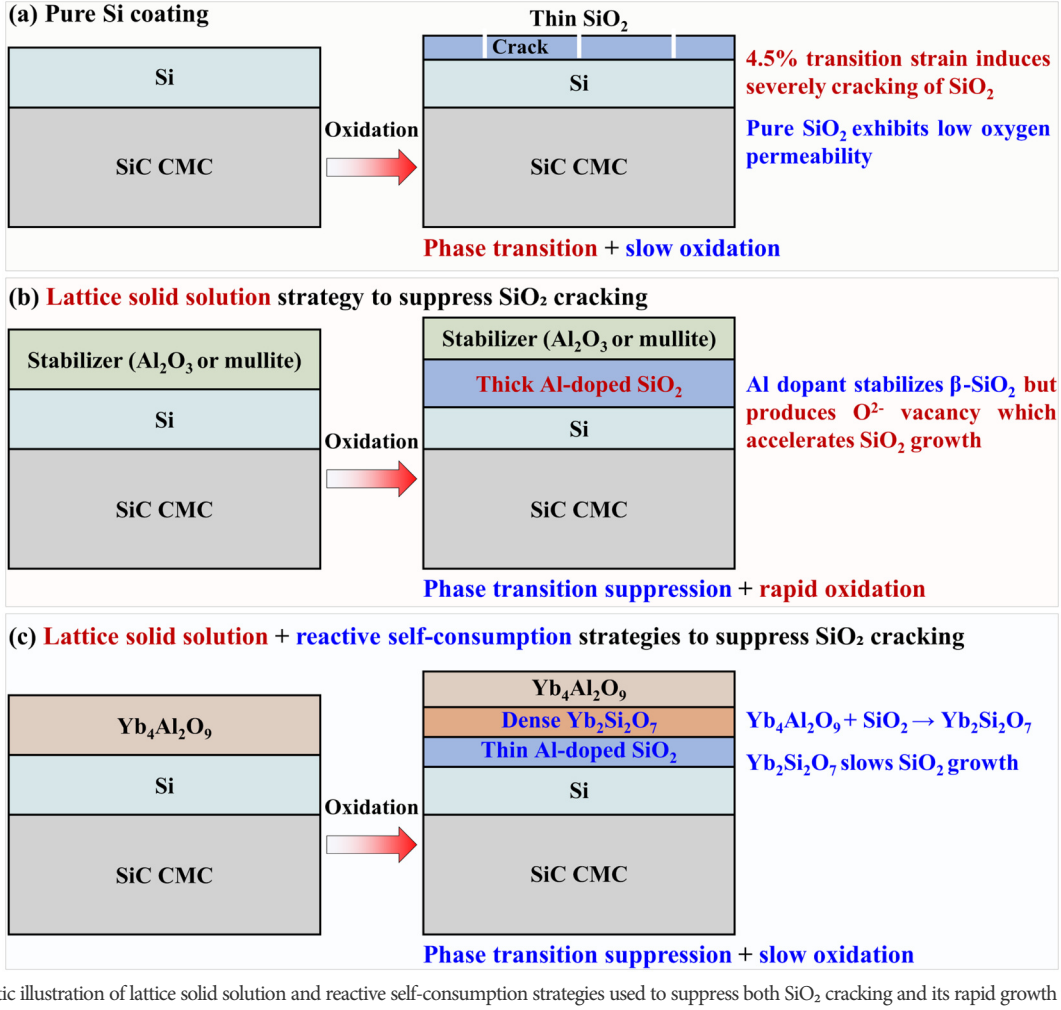

Fig. 1 Schematic illustration of lattice solid solution and reactive self-consumption strategies used to suppress both SiO_2 cracking and its rapid growth via Si–$Yb_4Al_2O_9$ composite coatings.

Table 1 Atmospheric plasma spraying parameters used in this study

Parameter	Si	$Yb_4Al_2O_9$	Si–$Yb_4Al_2O_9$
Plasma arc power (kW)	32.0	39.0	32.0
Plasma gas (Ar) (L·min^{-1})	45.0	45.0	45.0
Auxiliary gas (H_2) (L·min^{-1})	5.0	7.0	7.0
Torch traverse speed (mm·s^{-1})	400.0	400.0	400.0
Spray distance (mm)	80.0	80.0	80.0
Powder feed rate (r·min^{-1})	3.0	3.0	3.0
Scanning step (mm)	3.0	3.0	3.0
Deposition temperature (°C)	700.0	700.0	700.0

SiC substrates were grit blasted with 24 mesh SiC grits to achieve an average roughness (Ra) of 5 μm. The SiC substrates were preheated to 700 °C via a copper plate heater positioned beneath the sample. The surface temperature of the substrate was monitored with a calibrated thermocouple. The thickness of each layer was maintained between 50 and 100 μm.

2.3 Isothermal oxidation

The isothermal oxidation test was conducted in a high-temperature muffle furnace at 1370 °C under atmospheric conditions. During the isothermal oxidation process, the samples were placed in a corundum crucible and covered with another crucible to prevent contamination from environmental impurities. To determine the oxidation kinetics of the Si–$Yb_4Al_2O_9$ composite coatings, the isothermal durations were set to 10, 30, 50, 100, and 200 h. The samples were initially heated to 1370 °C at a heating rate of 5 °C·min^{-1} and then maintained at this temperature for the specified durations. After the holding period, the samples were cooled to room temperature at a cooling rate of 5 °C·min^{-1}. The coatings oxidized at 1300 °C served as the baseline for comparison.

2.4 Adhesion strength

Adhesion strength testing was conducted in accordance with the ASTM C-633 standard using an universal testing machine (Instron 1195, INSTRON Co., USA) at a constant speed of 1.0 mm·min^{-1}. The coated sample was first adhered to the dual parts via AB glue (302 modified acrylate adhesive, GELIAHAO, China). The mass ratio of AB glue was 1 : 1. The mixture was then subjected to osmotic curing at 100 °C for 3 h. Statistical values were derived from three samples within each group.

2.5 Microstructural characterizations

The surface and cross-sectional microstructures of the coatings were observed by a scanning electron microscope (SEM; VEGA II-XMU, TESCAN, Switzerland). The elemental distributions of the coatings were analyzed through energy dispersive spectroscopy (EDS; AZTEC, Oxford Instruments, UK) and an electron probe microanalyzer (EPMA; JXA-8230, JEOL, Japan). For EDS, an acceleration voltage of 15 kV and a working distance of 15 mm were employed. EPMA mapping was conducted with a step size of 0.3 μm and a mapping time of 15 ms. The phase compositions were identified via an X-ray diffractometer (XRD; D8 Advance 3.0, Bruker, USA), with a 2θ range of 10°–90°. The scanning step size was set to 0.1°, and the scanning speed was 2°·min^{-1}. Surface roughness (Ra) was assessed via a 3D confocal laser microscope (OLS5100, Olympus IMS, Japan), with statistical values calculated from ten positions per group. Furthermore, the thickness of the oxide scale was measured via Demo VegaTC software integrated into the SEM at a magnification of 10,000×; at least 100 measurements were taken per sample. The measurement direction was the normal direction of the TGO interface.

The atomic structures were investigated through a scanning transmission electron microscope (FSTEM; JEM-F200, JEOL, Japan, operating at 200 kV). The TEM samples were prepared via a focused ion beam (FIB; Quanta 200 FEG, FEI). The amorphous layers generated during FIB preparation were removed via a nanomill (M1040 Nano Mill, Fischione, USA) with argon ions (Ar^+) as the cleaning agent at an ion energy of 700 eV and a milling angle of 30°. The faces of the samples were milled for 30 min.

3 Results

3.1 As-sprayed coating structure

Figure 2 shows the microstructures of the as-sprayed Si–$Yb_4Al_2O_9$ coatings. Owing to gas entrapment during the deposition process [26], the coatings exhibit numerous splashed particles (Fig. 2(b)). The surface roughness of the duplex coating was measured at 14 μm, which is greater than that of the pure Si coating (7 μm). A surface roughness of 3.2 μm was reported for the Si coating [27]. Additionally, channel cracks were observed (Fig. 2(c)), which were attributed to deposition stress [13,15,28]. The deposition temperature significantly affects the bonding and porosity of the coating [29]. Given that the melting point of $Yb_4Al_2O_9$ is 2030 °C [23], a dense structure formed at a deposition temperature of 700 °C (Fig. 2(c)). A deposition temperature of 1200 °C was reported for the preparation of dense Yb_2SiO_5 [5,13,28] and $Yb_2Si_2O_7$ [12] environmental barrier coatings. Furthermore, the adhesion strength of the dual coating was measured at 30±3 MPa, which is 1.5 times greater than that of the pure Si coating. Figure 3 shows the XRD patterns of the as-sprayed Si–$Yb_4Al_2O_9$ coatings at room temperature, revealing the presence of $Yb_4Al_2O_9$ (major phase) and Yb_2O_3 (minor phase), with the latter likely originating from the $Yb_4Al_2O_9$ powder.

3.2 Structural evolution during oxidation

Figure 4 shows the surface morphologies of the pure Si coating after oxidation at 1370 °C. After 2 h of oxidation, continuous mud cracks were observed with a SiO_2 TGO thickness of approximately

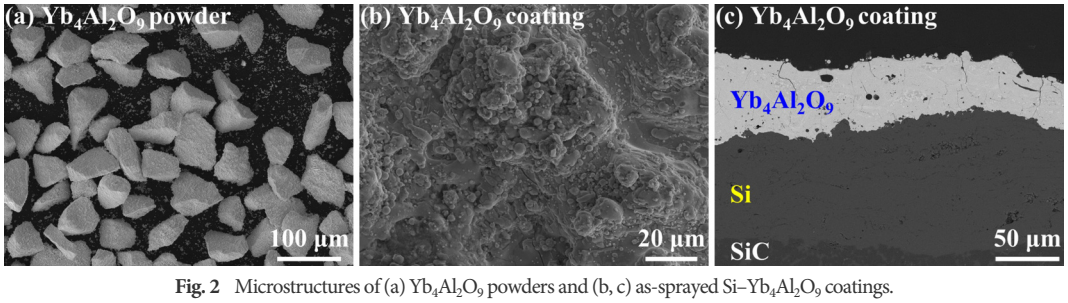

Fig. 2 Microstructures of (a) $Yb_4Al_2O_9$ powders and (b, c) as-sprayed Si–$Yb_4Al_2O_9$ coatings.

1.7 μm (Fig. 4(a)). This cracking is attributed to the β → α phase transition of SiO_2 TGO at approximately 220 °C, which causes a volumetric contraction of approximately 4.5% [15,17]. Channel cracking is reported to occur when the TGO thickness exceeds approximately 1.5 μm [12,17]. After 5 h of oxidation, the crack width increased, and the crack spacing decreased (Fig. 4(b)), indicating intensified stress [18]. After 10 h of oxidation, spallation occurred with a TGO thickness of approximately 3.8 μm, which is consistent with reports of delamination starting at TGO thicknesses of approximately 4 μm [14,17]. After 50 h of oxidation at 1370 °C, spallation affected 50% of the surface area, with a TGO thickness of approximately 9.0 μm. After 48 h of oxidation at 1300 and 1350 °C, the TGO thicknesses were reported to be 3.5 and 8.7 μm, respectively [17,26]. This study defines the oxidation lifetime on the basis of the integrity of SiO_2 TGO (the occurrence of spallation), which reflects its ability to protect against oxidation. Consequently, the oxidation lifetime of the pure Si coating at 1370 °C is approximately 10 h. These findings underscore the poor oxidation resistance of the pure Si coating at 1370 °C, which is primarily due to significant cracking and spalling induced by SiO_2 TGO phase transitions.

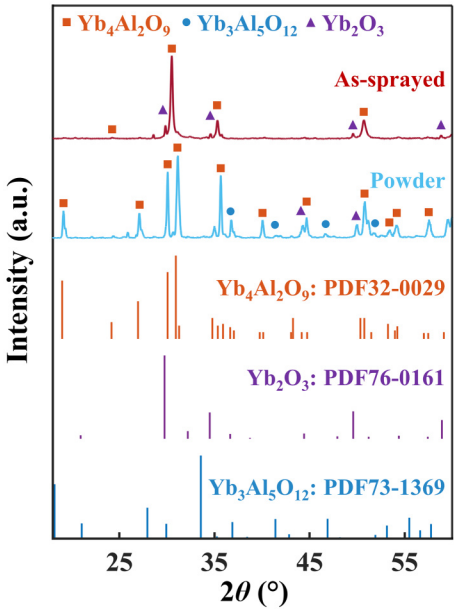

Fig. 3 XRD patterns of as-sprayed Si–$Yb_4Al_2O_9$ duplex coatings at room temperature.

Figure 5 shows the XRD patterns of the Si–$Yb_4Al_2O_9$ duplex coatings at room temperature. After oxidation at 1370 °C, phase decomposition of $Yb_4Al_2O_9$ occurred (Fig. 5(a)), resulting in the formation of Yb_2O_3 (major) and $Yb_3Al_5O_{12}$ (minor). After 10 h of oxidation at 1370 °C, diffraction peaks corresponding to the $Yb_2Si_2O_7$ phases appeared (Fig. 5(b)), indicating a reaction between SiO_2 and Yb_2O_3. $Yb_2Si_2O_7$ has a similar CTE to SiC and SiO_2 but much higher water vapor corrosion resistance [12,30], thus contributing to improving the service lifetime. These results indicate that $Yb_2Si_2O_7$ formed during the oxidation of the Si–$Yb_4Al_2O_9$ duplex coatings.

Figure 6 shows the cross-sectional microstructures of the Si–$Yb_4Al_2O_9$ duplex coatings after oxidation at 1300 and 1370 °C.

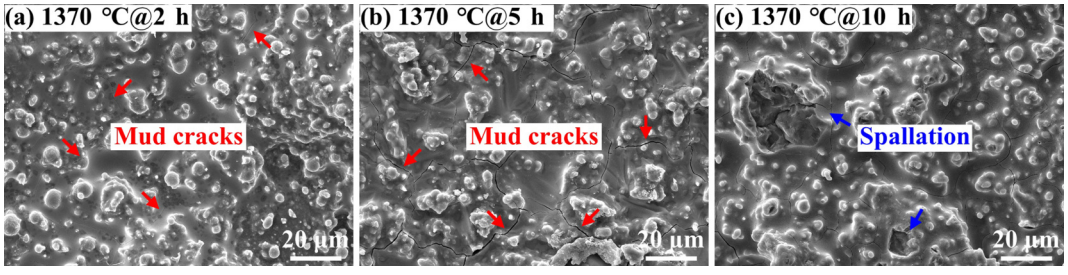

Fig. 4 Surface morphologies of pure Si coatings after oxidation for (a) 2 h, (b) 5 h, and (c) 10 h at 1370 °C.

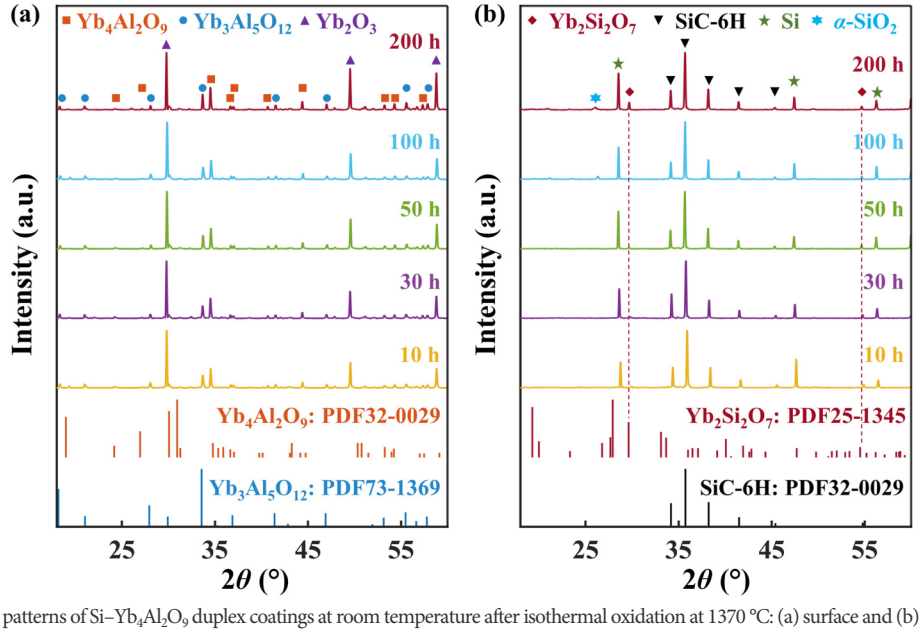

Fig. 5 XRD patterns of Si–$Yb_4Al_2O_9$ duplex coatings at room temperature after isothermal oxidation at 1370 °C: (a) surface and (b) cross section.

No spallation occurred after 200 h of oxidation at 1370 °C, with a TGO thickness of 6 μm (Fig. 6(f)). However, for pure Si coatings, delamination occurs when the TGO thickness reaches approximately 4 μm [14,17]. Furthermore, a continuous $Yb_2Si_2O_7$ layer formed between $Yb_4Al_2O_9$ and SiO_2 TGO (Figs. 7 and 8), which has a greater fracture toughness than SiO_2 does (Table 2). The *in situ* formed $Yb_2Si_2O_7$ layer was dense without pores or cracks, which could further prevent the spread of air to the bond coat. The formation of the $Yb_2Si_2O_7$ layer reduced the SiO_2 thickness, thus enhancing the cracking resistance. Moreover, $Yb_2Si_2O_7$ has a similar CTE to SiC and SiO_2 but much higher water vapor corrosion resistance, thus contributing to improving the service lifetime of the EBCs. These results indicate that the current dual coating design can suppress the phase transition of SiO_2 TGO during cooling. The oxidation lifetime of the current duplex coating exceeded 200 h at 1370 °C in this study. Compared with the 10 h oxidation lifetime of the pure Si coating, the lifetime of the duplex coating increased by more than 20 times.

3.3 TGO composition

Figures 7 and 8 show the elemental distribution on the Si–$Yb_4Al_2O_9$ duplex coatings after 200 h of oxidation at 1370 °C. Consistent with the XRD results (Fig. 5(a)), phase decomposition was observed on the coating surface (Fig. 7(a)). The top coat exhibited a composite structure of discrete $Yb_4Al_2O_9$ and $Yb_3Al_5O_{12}$ "bricks" embedded in a continuous Yb_2O_3 "mortar".

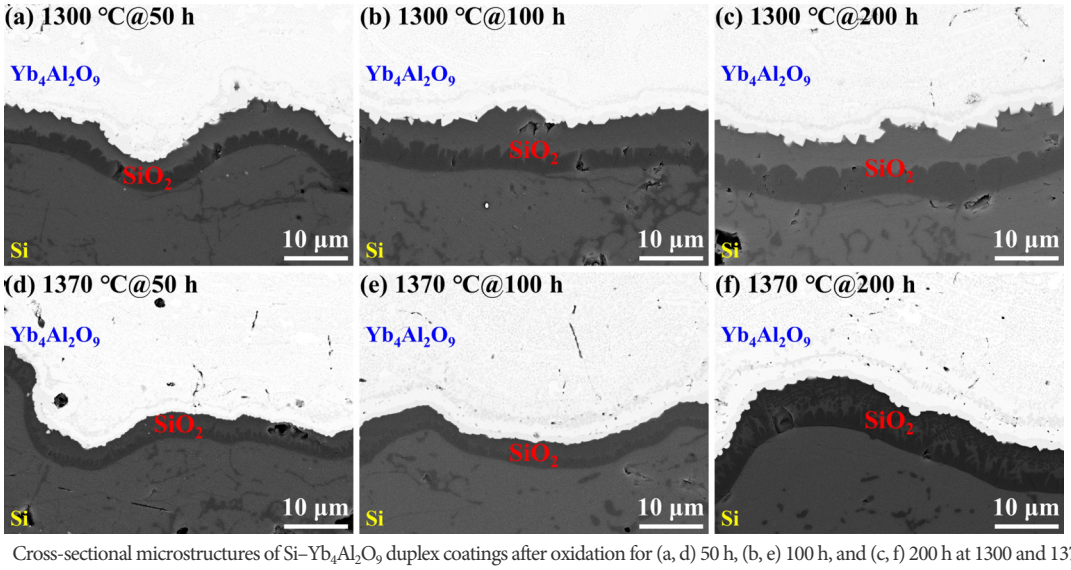

Fig. 6 Cross-sectional microstructures of Si–$Yb_4Al_2O_9$ duplex coatings after oxidation for (a, d) 50 h, (b, e) 100 h, and (c, f) 200 h at 1300 and 1370 °C.

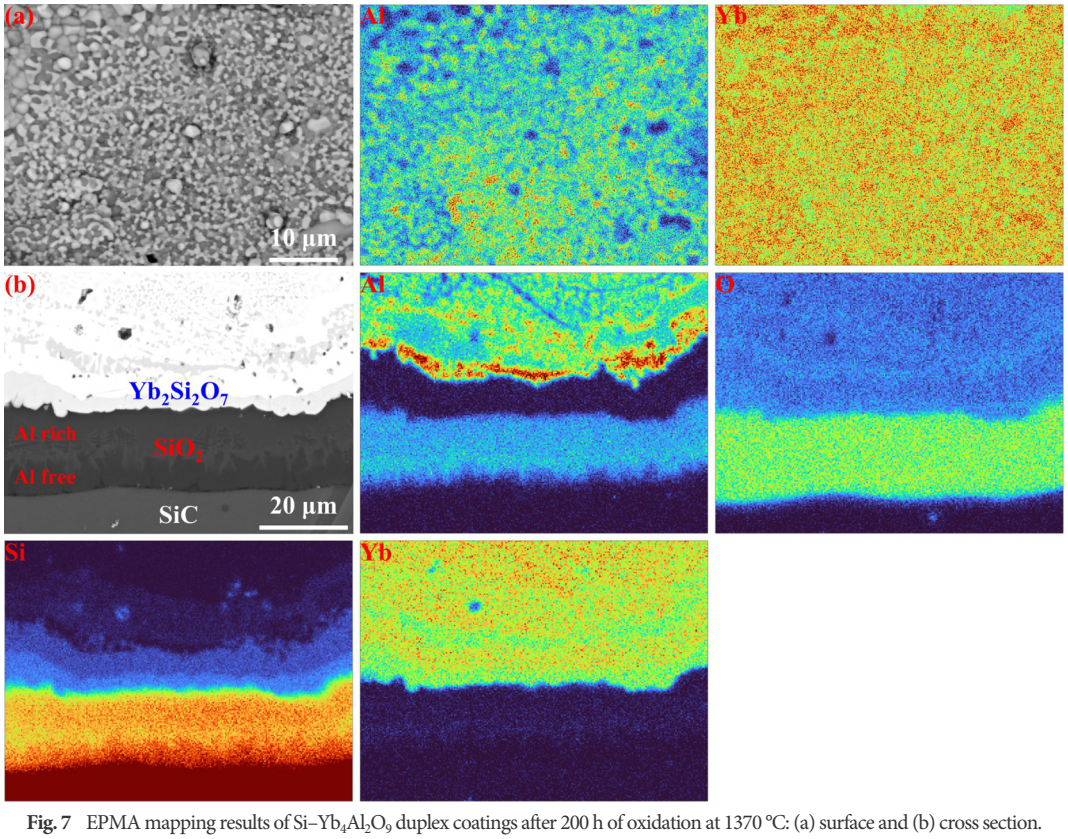

Fig. 7 EPMA mapping results of Si–$Yb_4Al_2O_9$ duplex coatings after 200 h of oxidation at 1370 °C: (a) surface and (b) cross section.

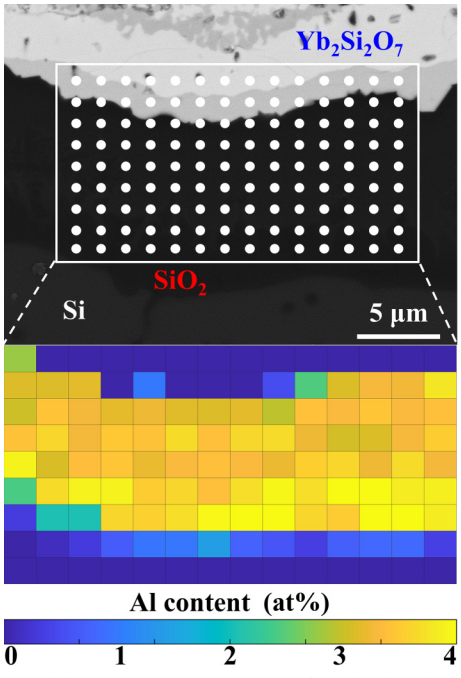

Fig. 8 Elemental distribution on cross section of Si–$Yb_4Al_2O_9$ duplex coatings after 200 h of oxidation at 1370 °C by EDS point analysis.

Table 2 presents the thermophysical properties of the current coating components. Although $Yb_3Al_5O_{12}$ has a higher CTE than SiC and SiO_2 do [31], it has superior fracture toughness and damage tolerance [32]. Like $HfSiO_4/SiO_2$ composites formed in Si–HfO_2 coatings [18], this $Yb_3Al_5O_{12}/Yb_2O_3$ composite structure has high cracking resistance. Moreover, $Yb_3Al_5O_{12}$ has a significantly lower oxygen diffusion coefficient [10] and greater water vapor corrosion resistance than SiC and SiO_2 [33]. In the Si–$Yb_2Si_2O_7$-HfO_2 EBC system [34,35], the dissolution of HfO_2 to $Yb_2Si_2O_7$ causes premature interfacial delamination. In contrast, both Yb_2O_3 and $Yb_3Al_5O_{12}$ can form stable interfaces with $Yb_2Si_2O_7$ (Figs. 6 and 7), thus suppressing interfacial delamination.

The SiO_2 TGO region was divided into two layers (Fig. 7(b)). The layer adjacent to the $Yb_4Al_2O_9$ layer was rich in Al, whereas the layer near the SiC substrate was poor in Al, indicating the diffusion of Al from the $Yb_4Al_2O_9$ layer into the SiO_2 layer. The Al content in the former was 4 at% (Fig. 8). Al doping aids high-temperature β-SiO_2 in retaining metastability at room temperature [17,36,37], thus preventing phase transition-induced cracking. These results indicate that Al-doped SiO_2 formed during the oxidation of the Si–$Yb_4Al_2O_9$ composite coatings, thereby preventing phase transition-induced cracking.

3.4 Si oxidation

The growth of SiO_2 TGO relies on oxidant diffusion, following parabolic growth kinetics as Eq. (1) [17,18,26,27,41]:

$$h = k_{gb}\sqrt{t} \tag{1}$$

where h is the TGO thickness (μm), t is the oxidation time (h), and k_{gb} is the oxidation rate (μm·h$^{-1/2}$). The oxidation rates for the pure Si and Si–$Yb_4Al_2O_9$ coatings are 1.16 and 0.44 μm·h$^{-1/2}$ at 1370 °C, respectively (Fig. 9(a)). Moreover, the oxidation rate of the pure Si coating increases significantly with temperature due to enhanced oxidant diffusion [17], a trend also observed in Si–HfO_2 composite coatings [18,19]. Interestingly, at 1370 °C, the TGO thickness is lower than that at 1300 °C (Fig. 9(a)). Conversely, the $Yb_2Si_2O_7$ thickness at 1370 °C exceeds that at 1300 °C (Fig. 9(b)). Apparently, the abnormal growth of SiO_2 is solely due to the formation of $Yb_2Si_2O_7$. These results confirm that $Yb_2Si_2O_7$ formation significantly reduces the SiO_2 growth rate in this study. This reduction is attributed to the fact that $Yb_2Si_2O_7$ possesses an oxygen diffusion coefficient comparable to that of SiO_2 and Al_2O_3 [25], which serves as an effective oxygen diffusion barrier.

The formation of 1 mol of $Yb_2Si_2O_7$ consumes 2 mol of SiO_2. Therefore, the equivalent SiO_2 thickness corresponding to the $Yb_2Si_2O_7$ layer is given by Eq. (2):

$$h_{Yb_2Si_2O_7-SiO_2} = \frac{2\rho_{Yb_2Si_2O_7}\cdot h_{Yb_2Si_2O_7}\cdot M_{SiO_2}}{M_{Yb_2Si_2O_7}\cdot \rho_{SiO_2}} \tag{2}$$

where $\rho_{Yb_2Si_2O_7}$, $h_{Yb_2Si_2O_7-SiO_2}$, and $M_{Yb_2Si_2O_7}$ are the density, the thickness, and the molar mass of $Yb_2Si_2O_7$, respectively, and ρ_{SiO_2} and M_{SiO_2} are the density and the molar mass of SiO_2, respectively. The equivalent oxidation rates for the Si–$Yb_4Al_2O_9$ coatings are 0.70 and 0.53 μm·h$^{-1/2}$ at 1300 and 1370 °C, respectively. The equivalent TGO thickness at 1370 °C remains lower than that at 1300 °C, highlighting the advantages of this coating for high-temperature applications. The reciprocal of growth rates serves as an indicator of oxidation resistance [42]. Figure 9(c) compares this value for current and previously reported coatings, demonstrating the superior oxidation resistance of the current system at 1370 °C. These findings emphasize the potential of the Si–$Yb_4Al_2O_9$ duplex as an EBC bond coating.

3.5 $Yb_2Si_2O_7$ formation

In this study, a dense and continuous $Yb_2Si_2O_7$ layer formed between the $Yb_4Al_2O_9$ layer and the SiO_2 layer (Figs. 7 and 8). The temperature significantly impacts the formation rate of the $Yb_2Si_2O_7$ layer (Fig. 9(b)). This occurred because the formation of $Yb_2Si_2O_7$ is governed by the diffusion of Si^{4+} through the $Yb_2Si_2O_7$ layer [43]. It has been reported that a thin layer of $Yb_2Si_2O_7$ forms

Table 2 Thermophysical properties of the current EBC system components [12,13,38–40]

Material	Modulus, E (GPa)	Poisson ratio, ν	Thermal expansion, α (10^{-6} K^{-1})	Fracture toughness, K_{IC} (MPa·m$^{1/2}$)	Thermal mismatch, ε_0 (%)
$Yb_4Al_2O_9$	151	0.280	6.27	3.36	0.216
Yb_2O_3	100	0.300	8.10	1.81	0.463
$Yb_3Al_5O_{12}$	282	0.240	7.50	2.88	0.382
$Yb_2Si_2O_7$	180	0.270	4.10	2.00	−0.077
Yb_2SiO_5	172	0.270	7.50	0.96	0.382
β-SiO_2	70	0.042	3.10	0.77	−0.177
α-SiO_2	65	0.164	30.00	0.77	0.507
Si	163	0.223	4.10	1.00	−0.077
SiC	430	0.140	4.67	3.30	—

in both Si/Yb_2SiO_5 and Si/mullite/Yb_2SiO_5 coatings [43–46]. The $Yb_2Si_2O_7$ layer exerts a pinning effect at the interface, thereby significantly enhancing the bonding strength and resistance against wet oxygen [44]. The thicknesses of the $Yb_2Si_2O_7$ layer in the Si/Yb_2SiO_5/$(Gd_{0.9}Yb_{0.1})_2Zr_2O_7$ coatings reached 1–3 and 2–7 μm after 500 h of oxidation at 1300 and 1370 °C, respectively, whereas the SiO_2 TGO thicknesses were only 3–5 and 5–7 μm [45]. These results confirm that a dense and continuous $Yb_2Si_2O_7$ layer can be formed *in situ*, which is conducive to reducing the SiO_2 growth rate.

The formation of the $Yb_2Si_2O_7$ layer offers several advantages: (1) Compared with the SiC substrate, the $Yb_2Si_2O_7$ layer has a lower CTE (Table 2), resulting in the development of compressive stress within the $Yb_2Si_2O_7$ layer during thermal cycling, which is beneficial for suppressing crack propagation. (2) It has greater fracture toughness than SiO_2 does (Table 2), further inhibiting crack propagation. (3) $Yb_2Si_2O_7$ has an oxygen diffusion coefficient comparable to those of SiO_2 and Al_2O_3 [25], significantly reducing the oxidation rate. (4) $Yb_2Si_2O_7$ is much more resistant to water vapor corrosion than both SiC and SiO_2 [12], significantly improving the corrosion resistance of the bond coating. These findings indicate that a dense and continuous $Yb_2Si_2O_7$ layer is advantageous for suppressing crack propagation and reducing oxidant permeation.

4 Discussion

4.1 Phase separation between $Yb_2Si_2O_7$ and SiO_2

To further demonstrate the contribution of the $Yb_2Si_2O_7$ phase to decreasing the oxidation rate, a Si–$Yb_4Al_2O_9$ composite coating with 15 vol% $Yb_4Al_2O_9$ was prepared. Figure 10 shows the

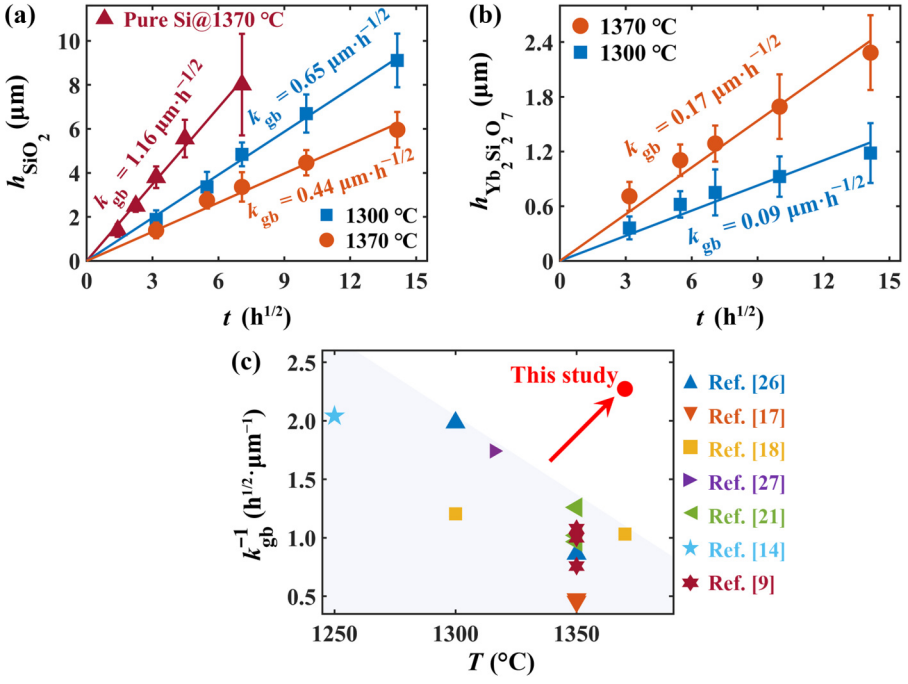

Fig. 9 Reaction kinetics of Si–$Yb_4Al_2O_9$ duplex coatings at 1370 °C: (a) SiO_2 thickness versus oxidation time; (b) $Yb_2Si_2O_7$ thickness versus oxidation time; (c) comparison of the reciprocal of SiO_2 growth rate in this work with those in other studies. The blue and orange lines in (a, b) represent Si–$Yb_4Al_2O_9$ duplex coatings oxidized at 1300 and 1370 °C, respectively. The red line in (a) represents pure Si coatings oxidized at 1370 °C.

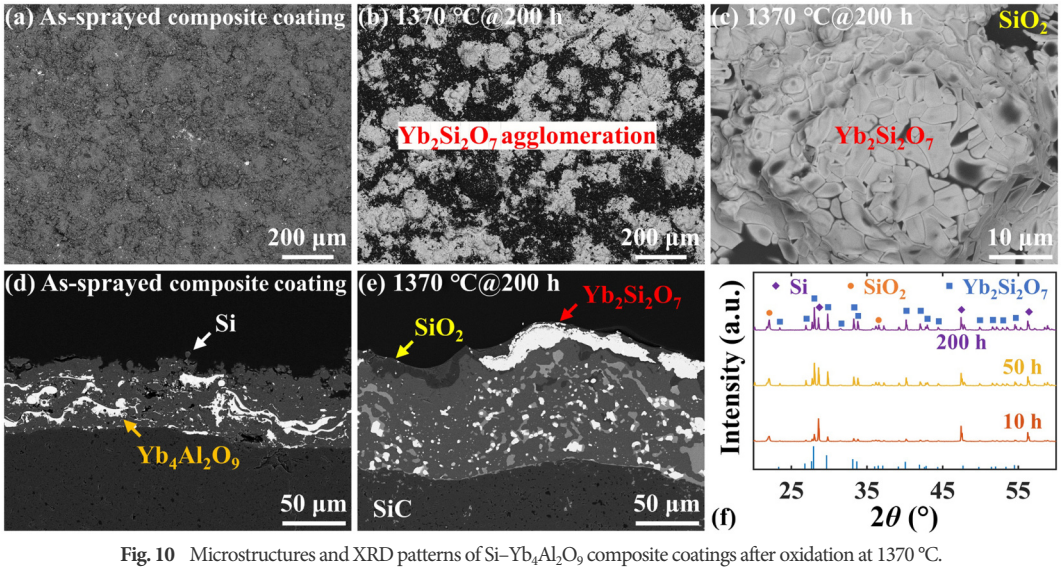

Fig. 10 Microstructures and XRD patterns of Si–$Yb_4Al_2O_9$ composite coatings after oxidation at 1370 °C.

microstructures of the Si–$Yb_4Al_2O_9$ composite coatings after oxidation at 1370 °C. In the as-sprayed coating, the $Yb_4Al_2O_9$ phase exhibited a discrete distribution (Figs. 10(a) and 10(d)). However, after oxidation at 1370 °C, the $Yb_2Si_2O_7$ phase became abundant on the coating surface (Figs. 10(b) and 10(e)), with a grain size of approximately 5 μm (Fig. 10(c)). In contrast to those of the duplex coatings (Fig. 5(a)), diffraction peaks associated with $Yb_2Si_2O_7$ were evident after 10 h of oxidation at 1370 °C on the coating surface (Fig. 10(f)). These observations suggest that phase separation between $Yb_2Si_2O_7$ and SiO_2 occurred during oxidation. This phase separation is detrimental to the suppression of SiO_2 cracking in the composite coating but is advantageous for the formation of a dense $Yb_2Si_2O_7$ layer atop SiO_2 in the dual coating. These results indicate that the dual coating design is a better choice than the composite coating design because of the phase separation between $Yb_2Si_2O_7$ and SiO_2.

4.2 Synergistic effect between Si oxidation and $Yb_2Si_2O_7$ formation

In this study, both SiO_2 and $Yb_2Si_2O_7$ formed during the oxidation of the Si–$Yb_4Al_2O_9$ duplex coatings (Fig. 5). The formation of the $Yb_2Si_2O_7$ layer significantly reduced the SiO_2 thickness, thereby enhancing the cracking resistance. The possible pathways for $Yb_2Si_2O_7$ formation are as Reactions (3)–(6):

$$5Yb_4Al_2O_9+14SiO_2\rightarrow 2Yb_3Al_5O_{12}+7Yb_2Si_2O_7 \quad \Delta H=-766\ \text{kJ}\cdot\text{mol}^{-1} \tag{3}$$

$$5Yb_4Al_2O_9\rightarrow 7Yb_2O_3+2Yb_3Al_5O_{12} \quad \Delta H=-84\ \text{kJ}\cdot\text{mol}^{-1} \tag{4}$$

$$Yb_2O_3+2SiO_2\rightarrow Yb_2Si_2O_7 \quad \Delta H=-97\ \text{kJ}\cdot\text{mol}^{-1} \tag{5}$$

$$Yb_2O_3+SiO_2\rightarrow Yb_2SiO_5 \quad \Delta H=-65\ \text{kJ}\cdot\text{mol}^{-1} \tag{6}$$

$$Yb_2SiO_5+SiO_2\rightarrow Yb_2Si_2O_7 \quad \Delta H=-32\ \text{kJ}\cdot\text{mol}^{-1} \tag{7}$$

where ΔH represents reaction enthalpy. After 10 h of oxidation, the diffraction peaks of Yb_2O_3 and $Yb_3Al_5O_{12}$ were observed on the coating surface (Fig. 5(a)), indicating that Reaction (4) occurred first, followed by Reaction (5), forming $Yb_2Si_2O_7$, as evidenced by the diffraction peaks of $Yb_2Si_2O_7$ on the coating cross-section (Fig. 5(b)). A dense and continuous $Yb_2Si_2O_7$ layer is beneficial for suppressing crack propagation and oxidant permeation. In this study, the formation rate of SiO_2 was greater than that of $Yb_2Si_2O_7$ (Figs. 9(a) and 9(b)). This discrepancy occurred because the formation of $Yb_2Si_2O_7$ is governed by the diffusion of Si^{4+} ions through the $Yb_2Si_2O_7$ layer [43], whereas the formation of SiO_2 is controlled by the diffusion of O^{2-} ions through the SiO_2 layer [10,17]. The incorporation of Al^{3+} ions into the crystalline SiO_2 lattice results in the formation of additional oxygen vacancies, leading to a significantly higher formation rate of SiO_2 than of $Yb_2Si_2O_7$. Figure 11 shows the STEM images at the SiO_2/$Yb_2Si_2O_7$/$Yb_4Al_2O_9$ interfaces. Consistent with the XRD results (Fig. 5(b)), a dense and continuous $Yb_2Si_2O_7$ layer formed adjacent to the SiO_2 scale (Fig. 11(a)). Additionally, Yb_2SiO_5 and Yb_2O_3 were observed adjacent to the $Yb_2Si_2O_7$ layer (Fig. 11(b)), indicating the occurrence of Reactions (6) and (7). This is supported by the report that Yb_2SiO_5 reacts with SiO_2 to form $Yb_2Si_2O_7$ at temperatures up to 1250 °C [46]. These results

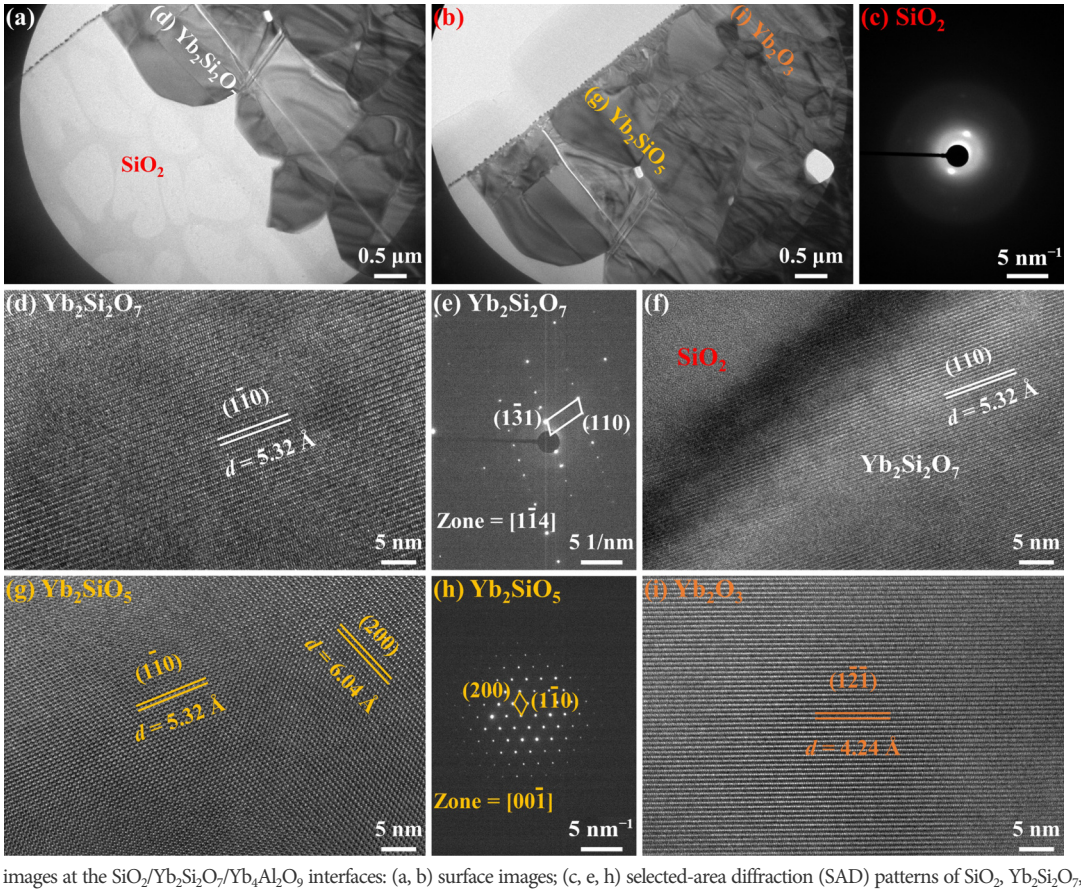

Fig. 11 STEM images at the SiO_2/$Yb_2Si_2O_7$/$Yb_4Al_2O_9$ interfaces: (a, b) surface images; (c, e, h) selected-area diffraction (SAD) patterns of SiO_2, $Yb_2Si_2O_7$, and Yb_2SiO_5; (d, g, i) HRTEM images of $Yb_2Si_2O_7$, Yb_2SiO_5, and Yb_2O_3; (f) HRTEM image at the SiO_2/$Yb_2Si_2O_7$ interface.

indicate that the Si–$Yb_4Al_2O_9$ duplex coatings transformed into SiO_2 and $Yb_2Si_2O_7$ simultaneously during isothermal oxidation.

One primary concern is the potential use of Yb_2O_3 or $Yb_3Al_5O_{12}$ as the reactive phases in the duplex bond coat. Although $Yb_3Al_5O_{12}$ has superior fracture toughness and damage tolerance (Table 2), it cannot react with SiO_2 (Reaction (3)) and therefore is unable to suppress the phase transition of SiO_2. While Yb_2O_3 can partially consume SiO_2 (Reaction (5)), the residual SiO_2 inevitably undergoes a phase transition. Consequently, neither Yb_2O_3 nor $Yb_3Al_5O_{12}$ is suitable as a reactive phase in the duplex bond coat.

4.3 Thermal stress-induced cracking

In addition to the volume contraction associated with the β → α phase transition (4.5%), the thermal mismatch between α-SiO_2 and SiC generates significant tensile stress within the α-SiO_2 layer during thermal cycling (Table 2). Channel cracking occurs when the thickness of α-SiO_2 exceeds approximately 1.5 μm [14,16], and spalling is observed along the α-SiO_2/Si interface when the thickness of α-SiO_2 reaches approximately 4 μm [14]. In contrast, β-SiO_2 has a lower CTE than SiC does, resulting in compressive stress within the β-SiO_2 layer (Table 2), which is beneficial for mitigating crack propagation. Therefore, facilitating the slow growth of β-SiO_2 is essential for alleviating both phase transition stress and thermal stress-induced cracking.

Similar to Si-stabilizer coatings [17], high-temperature β-SiO_2 retains its metastability at room temperature during the oxidation of Si–$Yb_4Al_2O_9$ composite coatings in this study (Figs. 7 and 8), thus preventing both phase transition stress and thermal stress-induced cracking. However, unlike the Si-stabilized coatings, the Si–$Yb_4Al_2O_9$ coatings presented oxidation rates comparable to those of the pure Si coatings (Fig. 9), further reducing their strain energy. This occurred because of the reaction between Yb_2O_3 and SiO_2 (Reactions (5) and (6)), forming a dense $Yb_2Si_2O_7$ layer with low oxygen permeability (Figs. 7–9). Consequently, the current coatings exhibited exceptional oxidation and cracking resistance.

Although β-SiO_2 TGO has a low cracking tendency, the decomposition of $Yb_4Al_2O_9$ results in additional failure risks. CTEs of the decomposition products Yb_2O_3 and $Yb_3Al_5O_{12}$ are 8.1×10^{-6} and 7.5×10^{-6} K^{-1}, respectively [39,40], which are greater than those of the SiC-CMCs (Table 2). This disparity may also cause cracking within the $Yb_4Al_2O_9$ top layer. Therefore, a future direction for the current design is to suppress the decomposition of $Yb_4Al_2O_9$.

In this study, the energy release rate (G) for channel cracking in the $Yb_4Al_2O_9$ top layer is given by Eq. (8):

$$G = g \cdot \frac{\varepsilon_0^2}{\bar{E}} \cdot d \tag{8}$$

where g is a dimensionless parameter (equal to 3.952 in this study), ε_0 is the thermal mismatch strain, $\bar{E}$ is the plane strain modulus, and d is the crack depth. Figure 12 shows the calculated energy release rate as a function of the crack depth. The energy release rate has an approximately linear relationship with crack depth when it is significantly less than the thickness of the top layer. However, as the crack approaches the $Yb_4Al_2O_9$/$Yb_2Si_2O_7$ interface, the energy release rate decreases, demonstrating that a dense and continuous $Yb_2Si_2O_7$ layer is beneficial for suppressing crack propagation.

Notably, the $Yb_4Al_2O_9$ coating exhibited a structure comprising discrete $Yb_4Al_2O_9$ and $Yb_3Al_5O_{12}$ "bricks" embedded in a continuous Yb_2O_3 "mortar" (Fig. 7(a)). Consequently, the cracking resistance of the current coating is much greater than that of the pure Yb_2O_3 coating, which is likely comparable to that of the pure $Yb_3Al_5O_{12}$ coating. Therefore, when the thickness of the $Yb_4Al_2O_9$ coating was less than 9 μm (Fig. 12), channel cracks could be avoided. Additionally, a dense $Yb_2Si_2O_7$ top layer was applied to the surface of the $Yb_4Al_2O_9$ layer in the actual EBC system, further reducing the cracking tendency of the $Yb_4Al_2O_9$ layer. These results indicate that the failure risk of the $Yb_4Al_2O_9$ layer can be mitigated by controlling its thickness in an actual EBC system.

4.4 Thermal stress-induced cracking

To address the SiO_2 phase transition, Si-stabilized composite coatings and Si–HfO_2 composite coatings have been proposed. In the case of Si-stabilizer composite coatings [17], the phase transition was suppressed through Al diffusion from the stabilizer into the SiO_2 scale. For Si–HfO_2 composite coatings [14,18,19], the phase transition was mitigated by the reaction between SiO_2 and HfO_2, resulting in the formation of $HfSiO_4$. However, both types of coatings exhibited rapid growth of the SiO_2 scale, which adversely led to cracking of the coating. The reactive self-consumption strategy introduced in this study has proven effective in suppressing both the SiO_2 phase transition and its rapid growth, providing a new direction for the design of next-generation durable EBCs.

This study presents a preliminary assessment of Si–$Yb_4Al_2O_9$ composite coatings for short-term, high-temperature applications (200 h at 1370 °C). However, for aerospace engine applications, further research is necessary to evaluate the thermal shock resistance and water vapor corrosion over extended service

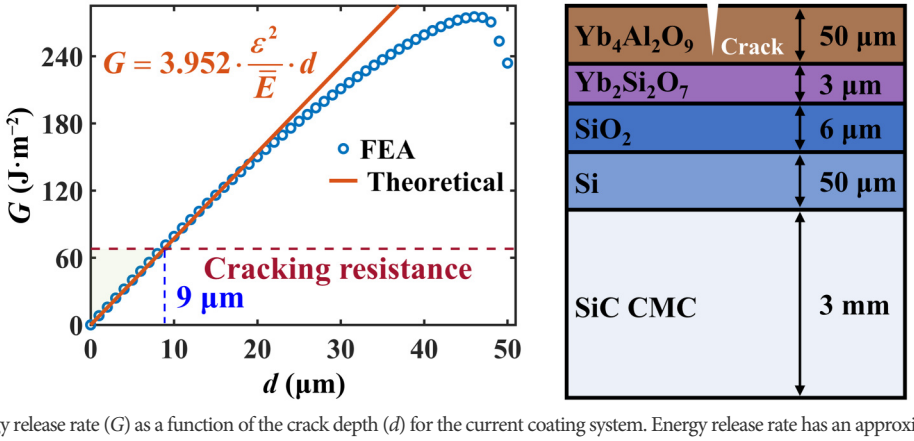

Fig. 12 Calculated energy release rate (G) as a function of the crack depth (d) for the current coating system. Energy release rate has an approximately linear relationship with crack depth when it is significantly less than thickness of $Yb_4Al_2O_9$ layer. However, as crack approaches $Yb_4Al_2O_9$/$Yb_2Si_2O_7$ interface, energy release rate decreases, indicating effectiveness of $Yb_2Si_2O_7$ layer in mitigating crack propagation.

periods. Addressing these challenges will be key to enhancing engine performance.

5 Conclusions

This study proposes reactive self-consumption and lattice solid solution strategies to suppress both the SiO_2 phase transition and its rapid growth via Si–$Yb_4Al_2O_9$ composite coatings. Structural evolution and oxidation kinetics were characterized, revealing the excellent oxidation and cracking resistance of the coatings. The main conclusions are as follows:

1) Lattice solid solution: Al incorporation into the SiO_2 lattice stabilizes high-temperature β-SiO_2, preventing phase transition-induced cracking.

2) Reactive self-consumption: The formation of $Yb_2Si_2O_7$ layer, through the consumption of SiO_2 and $Yb_4Al_2O_9$, reduces the SiO_2 thickness, significantly lowering the cracking driving force and enhancing the crack resistance.

3) Superior oxidation resistance: The proposed coating exhibited a service lifetime 20 times longer than that of pure Si at 1370 °C, underscoring its potential as an EBC bond coating.

Acknowledgements

The present project is supported by the National Postdoctoral Program for Innovative Talents (No. BX2021238) and the National Natural Science Foundation of China (No. 52401109).

Declaration of competing interest

The authors have no competing interests to declare that are relevant to the content of this article. The author Guan-Jun Yang is the Editorial Committee member of this journal.

References

[1] Padture NP. Advanced structural ceramics in aerospace propulsion. *Nat Mater* 2016, **15**: 804–809.

[2] Sun JX, Ye DR, Zou J, *et al.* A review on additive manufacturing of ceramic matrix composites. *J Mater Sci Technol* 2023, **138**: 1–16.

[3] Zhang GH, Shi JY, Zhang J, *et al.* Investigation on crystallization behavior between $(Sc_xYb_{1-x})O_{1.5}$ and CMAS: A new insight in the effect of Sc substitution. *J Adv Ceram* 2024, **13**: 789–799.

[4] Zhao ZF, Ruan ZY, Li R, *et al.* High entropy pyrochlore $(La_{0.3}Gd_{0.3}Ca_{0.4})_2(Ti_{0.2}Zr_{0.2}Hf_{0.2}Nb_{0.2}Ta_{0.2})_2O_7$ ceramic with amorphous-like thermal conductivity for environmental/thermal barrier coating applications. *J Mater Sci Technol* 2025, **205**: 315–326.

[5] Richards BT, Wadley HNG. Plasma spray deposition of tri-layer environmental barrier coatings. *J Eur Ceram Soc* 2014, **34**: 3069–3083.

[6] Lee KN, Zhu DM, Lima RS. Perspectives on environmental barrier coatings (EBCs) manufactured via air plasma spray (APS) on ceramic matrix composites (CMCs): A tutorial paper. *J Therm Spray Technol* 2021, **30**: 40–58.

[7] Turcer LR, Padture NP. Towards multifunctional thermal environmental barrier coatings (TEBCs) based on rare-earth pyrosilicate solid-solution ceramics. *Scripta Mater* 2018, **154**: 111–117.

[8] Kowalski B, Harder B. Thermally grown oxide in water vapor on coated and uncoated SiC. *J Am Ceram Soc* 2020, **103**: 5978–5989.

[9] Kane K, Garcia E, Stack P, *et al.* Evaluating steam oxidation kinetics of environmental barrier coatings. *J Am Ceram Soc* 2022, **105**: 590–605.

[10] Dong L, Yang WQ, Chen L, *et al.* Realizing the excellent oxidation resistance of an environmental barrier coating through aluminum surface modification. *J Adv Ceram* 2024, **13**: 976–986.

[11] Zhang PX, Duan XJ, Xie XC, *et al.* Xenotime-type high-entropy $(Dy_{1/7}Ho_{1/7}Er_{1/7}Tm_{1/7}Yb_{1/7}Lu_{1/7}Y_{1/7})PO_4$: A promising thermal/environmental barrier coating material for SiC_f/SiC ceramic matrix composites. *J Adv Ceram* 2023, **12**: 1033–1045.

[12] Richards BT, Young KA, de Francqueville F, *et al.* Response of ytterbium disilicate–silicon environmental barrier coatings to thermal cycling in water vapor. *Acta Mater* 2016, **106**: 1–14.

[13] Richards BT, Sehr S, de Franqueville F, *et al.* Fracture mechanisms of ytterbium monosilicate environmental barrier coatings during cyclic thermal exposure. *Acta Mater* 2016, **103**: 448–460.

[14] Anton R, Leisner V, Watermeyer P, *et al.* Hafnia-doped silicon bond Coats manufactured by PVD for SiC/SiC CMCs. *Acta Mater* 2020, **183**: 471–483.

[15] Bakan E, Vaßen R. Oxidation kinetics of atmospheric plasma sprayed environmental barrier coatings. *J Eur Ceram Soc* 2022, **42**: 5122–5128.

[16] Chen L, Li SW, Li CJ, *et al.* Promoting $Yb_2Si_2O_7$ environmental barrier coatings for service at 1425 °C. *J Eur Ceram Soc* 2025, **45**: 117200

[17] Chen L, Wang WJ, Li JH, *et al.* Suppressing the phase-transition-induced cracking of SiO_2 TGOs by lattice solid solution. *J Eur Ceram Soc* 2023, **43**: 3201–3215.

[18] Chen L, Luo JC, Yang WQ, *et al.* Durable dual-state duplex Si–HfO_2 with excellent oxidation and cracking resistance. *J Adv Ceram* 2024, **13**: 388–401.

[19] Harder BJ. Oxidation performance of Si–HfO_2 environmental barrier coating bond Coats deposited via plasma spray-physical vapor deposition. *Surf Coat Technol* 2020, **384**: 125311.

[20] Luo JC, Yang WQ, Chen L, *et al.* Silicon-based bond coatings for environmental barrier coatings: Present status and prospective. *Int J Appl Ceram Technol* 2024, **21**: 3771–3788.

[21] Ridley M, Kane K, Pint B. Environmental barrier coatings on SiC without a siliconbond coating: Oxidation resistance, failure modes, and future improvements. *J Korean Ceram Soc* 2024, **61**: 800–810.

[22] Yilmaz E, Paksoy AH, Gibson G, *et al.* Constrained sintering and thermal ageing behaviour of electrophoretically deposited $Yb_2Si_2O_7$ environmental barrier coating. *J Eur Ceram Soc* 2023, **43**: 6427–6439.

[23] Xiang HM, Feng ZH, Li ZP, *et al.* Crystal structure, mechanical and thermal properties of $Yb_4Al_2O_9$: A combination of experimental and theoretical investigations. *J Eur Ceram Soc* 2017, **37**: 2491–2499.

[24] Chen L, Yang B, Li GR, *et al.* Thermochemical stability of $Yb_2Si_2O_7$ environmental barrier coatings during thermal cycling and water vapor corrosion at 1350 °C. *J Therm Spray Technol* 2023, **32**: 1811–1827.

[25] Matsudaira T, Wada M, Kawashima N, *et al.* Mass transfer in polycrystalline ytterbium monosilicate under oxygen potential gradients at high temperatures. *J Eur Ceram Soc* 2021, **41**: 3150–3160.

[26] Chen L, Li JH, Wang GQ, *et al.* Improving oxidation resistance of Si coating by isolated-particle healing. *Corros Commun* 2022, **8**: 9–17.

[27] Chen DY. Suspension HVOF sprayed ytterbium disilicate environmental barrier coatings. *J Therm Spray Technol* 2022, **31**: 429–435.

[28] Richards BT, Begley MR, Wadley HNG. Mechanisms of ytterbium monosilicate/mullite/silicon coating failure during thermal cycling in water vapor. *J Am Ceram Soc* 2015, **98**: 4066–4075.

[29] Yao SW, Li CJ, Tian JJ, *et al.* Conditions and mechanisms for the bonding of a molten ceramic droplet to a substrate after high-speed impact. *Acta Mater* 2016, **119**: 9–25.

[30] McCormack S, Cao HT, Martins JP, *et al.* The effect of porosity, mixed molecular/Knudsen diffusion, and a surface barrier layer on steam corrosion of $Yb_2Si_2O_7$. *Corros Sci* 2023, **219**: 111238.

[31] Lu XR, Yuan JY, Li G, *et al.* Plasma-sprayed $Yb_3Al_5O_{12}$ as a novel thermal barrier coating for gas turbine applications. *J Eur Ceram Soc* 2024, **44**: 5138–5153.

[32] Wang XF, Xiang HM, Sun X, *et al.* Mechanical properties and damage tolerance of bulk $Yb_3Al_5O_{12}$ ceramic. *J Mater Sci Technol* 2015, **31**: 369–374.

[33] Paksoy AH, Martins JP, Cao HT, *et al.* Influence of alumina addition on steam corrosion behaviour of ytterbium disilicates for

environmental barrier coating applications. *Corros Sci* 2022, **207**: 110555.
[34] Deijkers JA, Begley MR, Wadley HNG. Failure mechanisms in model thermal and environmental barrier coating systems. *J Eur Ceram Soc* 2022, **42**: 5129–5144.
[35] Deijkers JA, Wadley HNG. A duplex bond coat approach to environmental barrier coating systems. *Acta Mater* 2021, **217**: 117167.
[36] Chao CH, Lu HY. Stress-induced β→α-cristobalite phase transformation in (Na_2O+Al_2O_3)-codoped silica. *Mater Sci Eng A* 2002, **328**: 267–276.
[37] Damby DE, Llewellin EW, Horwell CJ, *et al*. The α–β phase transition in volcanic cristobalite. *J Appl Crystallogr* 2014, **47**: 1205–1215.
[38] Wang X, Xue ZL, Zhou ZM, *et al*. Influence of $Yb_2Si_2O_7$ doping concentration on mechanical properties and thermal conductivity of Yb_2SiO_5–$Yb_2Si_2O_7$ composite ceramics. *J Alloys Compd* 2021, **889**: 161718.
[39] Zhong X, Niu YR, Li H, *et al*. Microstructure and thermomechanical properties of atmospheric plasma-sprayed Yb_2O_3 coating. *J Therm Spray Technol* 2018, **27**: 959–967.
[40] Zhou YC, Xiang HM, Feng ZH. Theoretical investigation on mechanical and thermal properties of a promising thermal barrier material: $Yb_3Al_5O_{12}$. *J Mater Sci Technol* 2014, **30**: 631–638.
[41] Chen L, Meng GH, Li CJ, *et al*. Critical scale grain size for optimal lifetime of TBCs. *J Mater Sci Technol* 2022, **115**: 241–250.
[42] Guo KY, Meng GH, Yang GJ. Enhanced oxidation resistance in Ti_3AlC_2 via selective self-healing. *J Eur Ceram Soc* 2024, **44**: 116676.
[43] Li G, Li JY, Lu XR, *et al*. Oxidation resistance and thermal shock behavior of tri-layer Si/Si–Yb_2SiO_5/Yb_2SiO_5–SiC environmental barrier coatings at 1300 °C. *Ceram Int* 2023, **49**: 13216–13226.
[44] Wang YL, Wang WL, Cao XX, *et al*. Failure behavior of SiC/SiC composites with Si/Yb_2SiO_5 and Si/mullite/Yb_2SiO_5 EBCs in wet oxygen at 1350 °C. *Int J Appl Ceram Technol* 2024, **21**: 358–369.
[45] Chen WB, He WT, He J, *et al*. Failure mechanisms of $(Gd_{0.9}Yb_{0.1})_2Zr_2O_7$/$Yb_2SiO_5$/Si thermal/environmental barrier coatings during thermal exposure at 1300 °C/1400 °C. *J Eur Ceram Soc* 2022, **42**: 3297–3304.
[46] Hu Q, Wang YC, Guo XJ, *et al*. Oxidation inhibition behaviors of environmental barrier coatings with a Si–Yb_2SiO_5 mixture layer for SiC_f/SiC composites at 1300 °C. *Surf Coat Technol* 2022, **438**: 128421.